# Dressing up Nanoparticles: A Membrane Wrap to Induce Formation of the Virological Synapse

Xinwei Yu,[†] Fangda Xu,[†] Nora-Guadalupe P. Ramirez,[‡] Suzanne D. G. Kijewski,[‡] Hisashi Akiyama,[‡] Suryaram Gummuluru,[*,‡] and Björn M. Reinhard[*,†]

[†]Department of Chemistry and The Photonics Center, Boston University, Boston, Massachusetts 02215, United States and [‡]Department of Microbiology, Boston University School of Medicine, Boston, Massachusetts 02118, United States

ABSTRACT Next-generation nanoparticle-based drug delivery systems require the ability to target specific organelles or subcellular regions in selected target cells. Human immunodeficiency virus type I (HIV-1) particles are evolutionarily optimized nanocarriers that have evolved to avoid intracellular degradation and achieve enrichment at the synapse between mature dendritic cells (mDCs) and T cells by subverting cellular trafficking mechanisms. This study demonstrates

that integration of the glycosphingolipid, GM3, in a membrane around a solid nanoparticle (NP) core is sufficient to recapitulate key aspects of the virus particle trafficking in mDCs. GM3-presenting artificial virus NPs (GM3-AVNs) accumulate in CD169^{+} and CD81^{+} nonlysosomal compartments in an actin-dependent process that mimics the sequestration of HIV-1. Live-cell optical tracking studies reveal a preferential recruitment and arrest of surface scanning CD4^{+} T cells in direct vicinity to the AVN-enriched compartments. The formed mDC—T cell conjugates exhibit strong morphological similarities between the GM3-AVN-containing mDC—T cell synapse and the HIV-1 virological synapse, indicating that GM3—CD169 interactions alone are sufficient for establishing the mDC—T cell virological synapse. These results emphasize the potential of the GM3-AVN approach for providing therapeutic access to a key step of the host immune response—formation of the synaptic junction between an antigen-presenting cell (mDC) and T cells—for modulating and controlling immune responses.
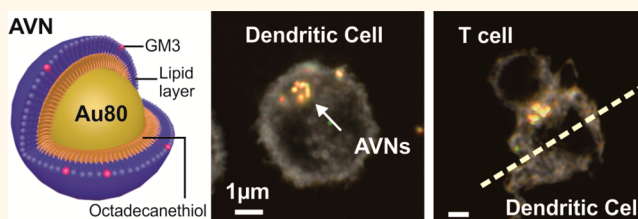
KEYWORDS: biomimetics · stealth nanoparticles · human immunodeficiency virus · drug delivery · glycosphingolipid · Siglec1 · GM3

The immunological synapse[1] defines an organized tight contact between an antigen-presenting cell, such as a dendritic cell (DC), and a lymphocyte, which plays an important role in ensuring an efficient communication between key components of the immune system. A series of diseases ranging from cancer[2] to autoimmune disorders[3] would benefit from a selective targeting of the immunological synapse with therapeutic nanoparticles (NPs) and delivery systems. Interestingly, human immunodeficiency virus type 1 (HIV-1) has evolved to subvert cellular trafficking and signaling mechanisms within DCs to achieve accumulation at the DC—T cell contact site.[4−7] These unique cell-to-cell contacts, termed virological synapses,[8] facilitate an efficient transmission of HIV-1 from DCs to CD4^{+} T cells, which are the preferred host cells of the virus.[9] In the case

of HIV-1, engagement of the sialoadhesin CD169, or Siglec1, expressed on mDCs by the terminal α2−3 sialylated ganglioside GM3 contained in the viral membrane is sufficient to trigger a localization of virus particles to the cellular periphery and, upon initiation of a mDC—T cell contact, induce their trafficking to the mDC—T cell virological synapse.[10−13] The GM3-CD169-mediated cellular uptake and trafficking mechanisms provide, therefore, unique opportunities for site-selective delivery with appropriately designed NP platforms. Site-selective delivery is crucial for surgical delivery approaches that achieve maximum efficacy and minimize collateral damage.[14]

Due to their complementarity in size with virus particles, colloidal NPs with rationally tunable surface properties have attracted significant interest as virus model systems that mimic specific functionalities

of the evolutionarily optimized virus particles for improved drug delivery.[15−17] Membrane-wrapped NPs,[18−23] in particular, are an emerging class of hybrid nanomaterials that combine the biological functionality of a lipid membrane with the advantageous photophysical,[23] multimodal,[19] or delivery properties[21] of an inorganic NP core for various theranostic applications. In this study we demonstrate that membrane-wrapped gold NPs successfully trigger GM3-CD169-dependent cellular trafficking mechanisms in mDCs and achieve an intracellular fate similar to HIV-1 particles. Using single-particle tracking analysis, we show that integration of GM3 into these artificial virus nanoparticles (AVNs)[23] is sufficient to achieve their preferential localization at the mDC−T cell synaptic junction, which shares strong molecular resemblances with the virological synapse. These findings highlight a number of potential advantages of the GM3-CD169 strategy, including targeting of a specific cell population (CD169-expressing macrophages and dendritic cells),[24] uptake *via* a nonlysosomal trafficking pathway, and the ability to modulate mDC−T cell signaling by selectively delivering therapeutic NPs to the mDC−T cell synaptic junction.

RESULTS AND DISCUSSION

AVNs were generated through a one-pot assembly strategy in which citrate-stabilized gold NPs were incubated with 1-octadecanethiol in the presence of liposomes of defined composition.[22,23] Due to the high affinity of the thiol residue to the gold surface, 1-octadecanethiol replaces the citrate and assembles into a 1-octadecanethiol monolayer around the gold NPs. The hydrophobic tails of the lipids readily integrate into this layer, completing the AVN assembly. The resulting AVN structure is schematically depicted in Figure 1a. For each AVN batch we validated the successful formation of a membrane around the gold NP core by inspection in the TEM (Figures 1b and S1), by monitoring the hydrodynamic radius of the particles through dynamic light scattering (DLS) (Figure 1c), and by quantifying the colocalization of the fluorescently labeled membrane with the NP scattering signal in correlated fluorescence/dark-field single-particle microscopy (Figure 1e). We also monitored the UV−vis of the NPs before and after membrane assembly (Figure 1d) to ensure that the AVN formation did not result in NP agglomeration. The absence of a red-shift confirms that the membrane assembly does not induce agglomeration. In fact, the AVN spectrum is even slightly sharper than that of the NP cores before membrane assembly, indicating a colloidal stabilization of the NPs due to membrane formation. A successful membrane assembly resulted in an increase of the average hydrodynamic NP diameter from 91 ± 1 nm to 102 ± 3 nm and yielded colocalization probabilities of >95%.

The HIV-1 membrane contains cholesterol, virus-encoded glycoproteins, and various host-cell-derived
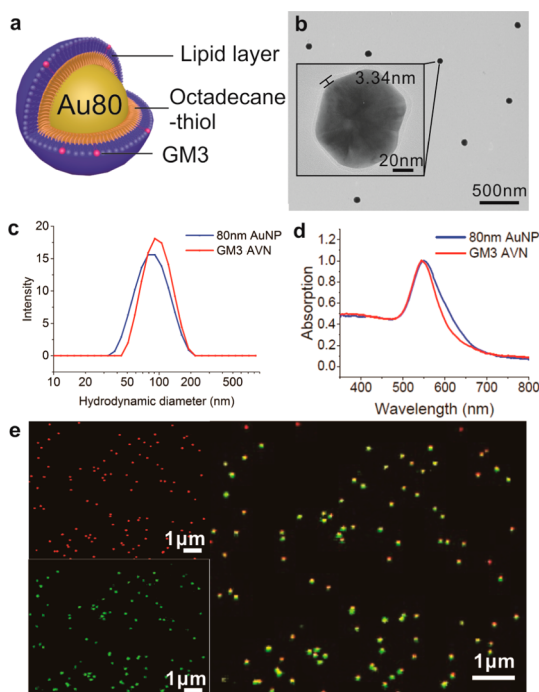

Figure 1. Characterization of GM3-containing AVNs. (a) Scheme of the AVN structure comprising a lipid monolayer anchored to the gold NP core through 1-octadecanethiol. (b) High-resolution TEM image of a representative GM3-AVN shows a visible membrane around the gold nanoparticle core, indicative of successful membrane assembly. (c) Hydrodynamic diameter (nm) of GM3-AVNs and 80 nm gold (Au) NPs (used as AVN core) measured by dynamic light scattering (DLS). (d) UV−vis spectra of GM3-AVNs and 80 nm gold NPs show peak wavelengths centered at 544 nm. (e) Dark-field image (red, top), fluorescent image (green, bottom), and superimposed image (right) confirm a strong colocalization (yellow) of the fluorescently labeled membrane and the gold NP core for immobilized GM3-AVNs. A colocalization level of approximately 96% indicates a highly efficient membrane wrapping of the gold NP core.

phospholipids and glycosphingolipids.[25,26] We used a simplified lipid membrane composition for the AVNs that comprised only dipalmitoylphosphatidylcholine (DPPC) and cholesterol as major components (Table S1). Phosphatidylserine (0.1 mol %) was added to maintain a virus-like surface charge ($\zeta \approx -25$ mV), and the inclusion of <0.1 mol % Topfluor-labeled cholesterol in the membrane allowed the detection of membrane formation through fluorescence microscopy. We included GM3 at a nominal concentration of 3 mol %. A characterization of the surface charge in DPPC/cholesterol/GM3-wrapped AVNs (Figure S2) indicated that this feeding ratio led to an effective concentration of ~1 mol % GM3 in the AVN membrane, which is in excellent agreement with the expected GM3 concentration in HIV-1. The resulting GM3-AVNs showed specific binding to CD169-expressing lipopolysaccharide (LPS)-activated DCs as determined by inductively coupled plasma mass spectroscopy (ICP-MS, Figure 2a), flow cytometry (Figure 2b), and optical cell binding studies (Figure S3).
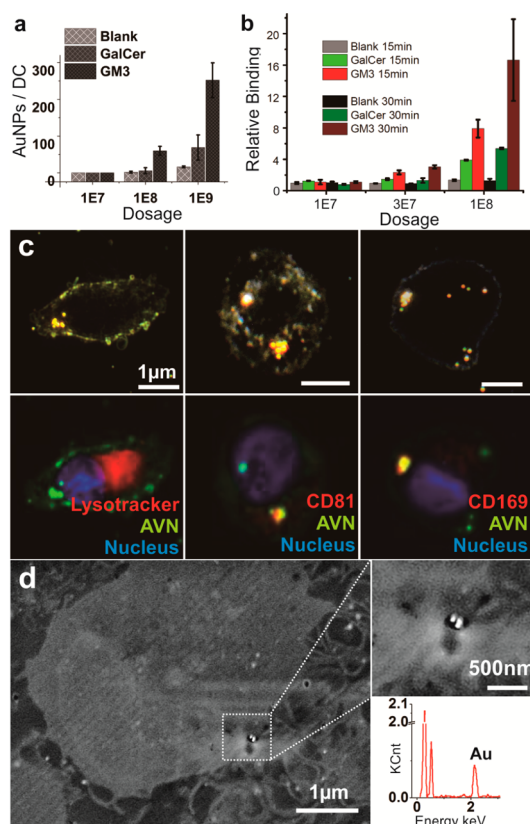
Figure 2. GM3-AVNs recapitulate GM3-CD169-mediated HIV-1 sequestration into peripheral nonlysosomal compartments in mDCs. (a) Mature DCs were challenged with GM3-AVNs, GalCer-AVNs, or blank controls at three different AVN/mDC ratios ($1 \times 10^7/3 \times 10^5$; $1 \times 10^8/3 \times 10^5$; $1 \times 10^9/3 \times 10^5$) for 5 min at 37 °C before the number of gold (Au) NPs (mean ± SD) bound per mDC was determined by ICP-MS. Data were collected in two independent experiments (two donors) for each dosage. The design of the AVNs is included in the inset. **(b)** Mature DCs were challenged with fluorescently labeled GM3-AVNs, GalCer-AVNs, or blank controls at three different AVN/mDC ratios ($1 \times 10^7/3 \times 10^5$; $3 \times 10^7/3 \times 10^5$; $1 \times 10^8/3 \times 10^5$) for 15 or 30 min at 37 °C before the mean fluorescence intensities were determined by flow cytometry. Data for each dosage represent means of duplicate measurements from one donor. **(c)** Staining of lysosomes (Lysotracker; top panel), CD81 (middle panel), and CD169 (bottom panel) in GM3-AVNs containing mDCs. The AVN/mDC ratio was $1 \times 10^8/3 \times 10^5$ and the incubation time was 1 h. Scale bars = 1 μm. **(d)** SEM of an mDC section shows a peripheral AVN cluster located close to the cell surface. The energy dispersive X-ray analysis (EDAX) (inset, left right corner) shows the elementary composition of the enlarged field, which confirms that the imaged NPs are gold NPs.

GM3-CD169-Mediated AVN Capture by mDCs. Our protein-free AVN design with a simple lipidome is ideally suited to investigate GM3's function in mediating HIV-1 capture and mDC–T cell virological synapse formation. Importantly, GM3-AVN binding to mDCs triggers unique uptake and trafficking mechanisms that result in the segregation of AVNs in peripheral nonlysosomal (Figure 2c, top row) and CD81^{+} (Figure 2c, middle row) compartments.[23] Immunofluorescence staining of CD169 (Figure 2c, bottom row) confirms now that these unique compartments are also enriched in

CD169, which provides further evidence of a GM3-CD169-binding-mediated segregation mechanism. We emphasize that the enrichment of CD169 at the site of GM3-AVN clustering in mDCs closely resembles the colocalization of CD169 with HIV-1 particles in CD81^{+} peripheral compartments.[10,13,23] Interestingly, these GM3-AVN-containing compartments resemble the recently described HIV-1-containing CD169^{+} plasma membrane invaginations in mDCs.[27] Since the wide-field optical images in Figure 2c do not provide specific information about the intracellular location of the AVN-enriched compartments, we prepared mDC sections for imaging in the scanning electron microscope (SEM). Figure 2d shows a representative SEM image of a cross-section of a GM3-AVN-treated mDC after an incubation period of 1 h. Numerous dendrites characteristic of mDCs are prominently seen, and a gold (Figure 2d, inset) AVN cluster was located just below the cell surface.

Together, the performed optical and electron microscopic studies verify that GM3-AVNs accumulate in CD81^{+} and CD169^{+} nonlysosomal compartments close to the cell surface. The segregation of GM3-AVNs in these unique compartments indicates a successful mimicry of the GM3-CD169-dependent trafficking of HIV-1 particles in mDCs.[28,29]

Characterization of GM3-AVN Motility and Clustering in mDCs. The optical properties of the 80 nm gold nanoparticle core of AVNs are determined by coherent electron oscillations (plasmons) whose resonances lie in the visible range of the electromagnetic spectrum.[30] Due to resonant light scattering, AVNs provide large scattering cross sections and can be imaged with high contrast and without blinking or bleaching on or in DCs under dark-field illumination.[31,32] We utilized the bright nature of the AVNs to experimentally address the kinetics of CD169-mediated clustering of GM3-AVNs in peripheral membrane compartments in mDCs. Mature DCs were incubated with GM3-AVNs ($1 \times 10^8/3 \times 10^5$ AVN/cell ratio) in serum-free growth medium at 37 °C for increasing time intervals (5, 15, 30, 45, and 60 min) before the AVNs were removed, and the spatial distribution of the AVNs on the single cell level was determined through dark-field microscopy.

We subdivided the AVN-treated cells into three groups (*No AVN*, *Cluster*, and *Random*) as defined in Figure 3a. The fraction of AVN-containing cells (sum of *Cluster* and *Random*) increases initially as a function of time (Figure 3b, green curve) and plateaus after approximately 20 min, when ~50% of all mDCs contain AVNs. We emphasize that this incomplete binding is not particular to AVNs. Similar binding levels are achieved with HIV-1 Gag virus like particles (VLPs),[12] and we rationalize this observation with variations in the Poisson-distributed CD169 expression level within primary cells (mDCs). The ratio of the *Cluster* and *Random* phenotypes (blue and red curves in Figure 3b) changes as a function of time. Within the first 10 min
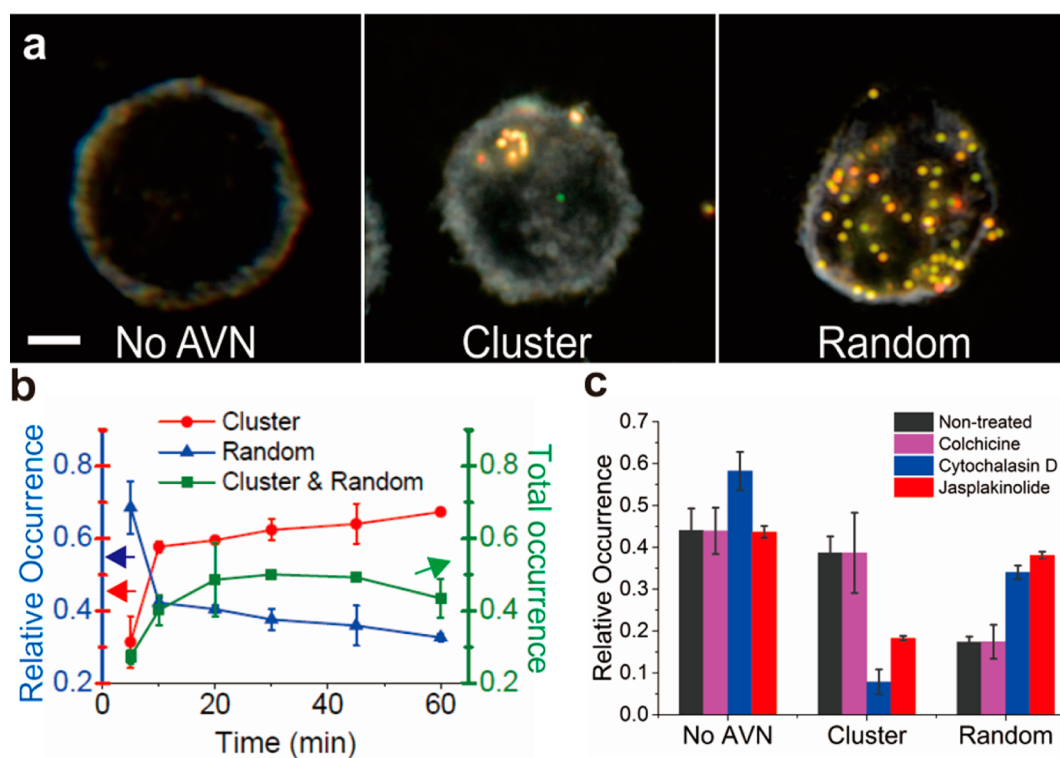
Figure 3. Characterization of the temporospatial GM3-AVN distribution in mDCs. (a) Illustration of the GM3-AVN distribution pattern observed: *No AVN* (left), *Cluster* (middle), and *Random* (right). Scale bar = 1 μm. (b) Fraction ($\pm$SD) of mDCs containing GM3-AVNs (green curve) and relative occurrence ($\pm$SD) of *Cluster* (red curve) *versus Random* phenotype (blue curve) in mDCs as a function of time. For each time point data were collected from >200 mDCs from three different donors in three independent experiments. (c) Relative occurrence of *No AVN*, *Cluster*, and *Random* phenotypes after treatment with colchicine, cytochalasin D, or jasplakinolide, as well as for the control without treatment. Presented data are averages ($\pm$SD) of two repeats from one donor.

the relative contribution from the *Cluster* phenotype increases sharply from 30% to 57% at the expense of the *Random* phenotype. Subsequently, the rate of conversion of the *Random* into the *Cluster* phenotype becomes more gradual with increasing time (after 60 min the *Cluster/Random* ratio is 68%/32%).

We found that actin-targeting pharmaceuticals, such as jasplakinolide, a macrocyclic peptide that inhibits actin filament depolymerization and induces monomer polymerization, as well as cytochalasin D, an actin polymerization inhibitor, suppress AVN clustering (Figure 3c). In contrast, treatment with the microtubule polymerization inhibitor colchicine had no effect. These observations indicate a key role for a dynamic cortical actin network in AVN clustering (*vide infra*).

To validate that the *Cluster* phenotype emanates from the *Random* phenotype, we monitored the spatiotemporal distribution of GM3-AVNs within individual cells. To that end, mDCs were initially incubated with GM3-AVNs for 10 min at 4 °C. The samples were then transferred into a dark-field microscope equipped with a cage incubator set at 37 °C, and all of the AVNs bound to the mDCs in the field of view were tracked simultaneously. Figure 4a shows two images of a GM3-AVN-containing mDC: one at the beginning of the image acquisition and another after 8 min 24 s.

The initially randomly distributed AVNs show an obvious coalescence, which is entirely consistent with the conversion of the *Random* into the *Clustered* phenotype. While we cannot exclude some degree of NP agglomeration in solution, especially at longer incubation times, the observation of AVN clustering in individual cells in real time together with the actin dependence of the clustering process (Figure 3c) indicates a GM3-triggered cellular response as the origin of the AVN segregation shown in Figure 3b.

Optical single virus tracking has become a reliable tool to obtain mechanistic information about virus uptake, trafficking, and transfer.[33−37] We reasoned that AVN tracking is equally well suited to provide additional mechanistic insight into the virus-clustering mechanism in mDCs. To visualize this trafficking mechanism in real time, we recorded movies of individual mDCs at different time points after AVN exposure in a dark-field microscope. We constructed trajectories for all of the AVNs detectable on the imaged mDC top surfaces and found a heterogeneous AVN motility characterized by different motion patterns at different time points. This effect can even be observed within individual trajectories. Figure 4b shows representative trajectories (approximately 20 s) of the AVNs marked as 1−6 in Figure 4a at selected time points. The starting
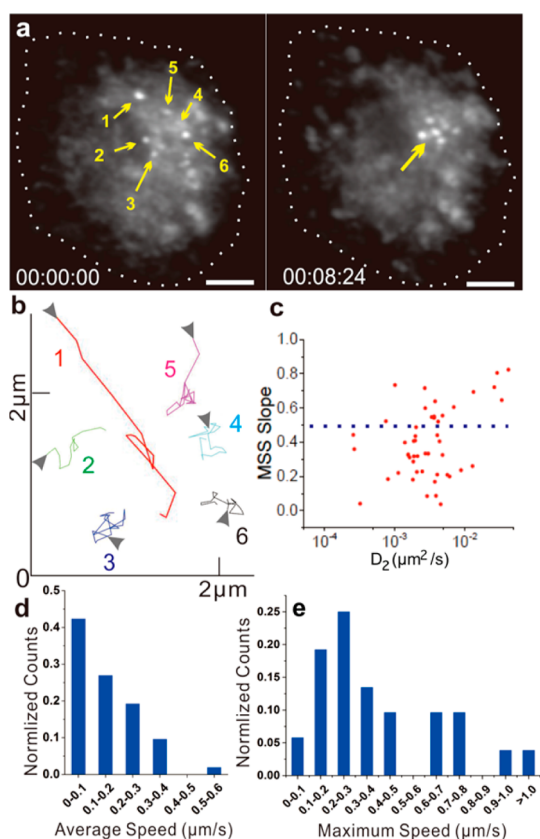
Figure 4. Real-time tracking of GM3-AVN in live mDCs. (a) Representative images of a GM3-AVN-containing mDC at $t = 0$ min and $t = 8$ min 24 s. Scale bar = 1 μm. **(b)** Trajectories (~20 s) of six GM3-AVNs in mDCs (yellow arrows in a). **(c)** Moment scaling spectrum (MSS) slopes (S_{MSS}) plotted as a function of diffusion coefficient D_2 for 52 trajectories. **(d)** Histogram of average speeds for the recorded trajectories. **(e)** Histogram of maximum speeds for the recorded trajectories.

points of the individual trajectories are marked by arrows. AVNs 1, 2, and 5 show obvious differences in their motility within the duration of the movie and contain segments of directed as well as of more random motion. To analyze the motion pattern of AVNs during the clustering process more systematically, we calculated the moment scaling spectra (MSS) introduced by Ferrari et al.[38] for a total of 52 trajectories with durations of approximately 20 s from 10 AVNs recorded on three different cells. The MSS slope (S_{MSS}) represents a quantitative metric for characterizing the motion of diffusing NPs, and S_{MSS} values of 0, 0.5, and 1 correspond to immobilized, free, and directed diffusion, respectively.[39,40] Figure 4c summarizes the obtained S_{MSS} values in a plot against the linear diffusion coefficient D_2. The average diffusion coefficient $D_2 = 5.5 \times 10^{-3}$ μm^2/s is significantly lower than for free NP diffusion on a membrane.[41] The S_{MSS} values show a broad distribution in the range between 0.02 and 0.82, confirming variations in the lateral motility between individual AVNs and for individual AVNs at different points in time. In particular, the motion patterns of

individual CD169-tethered GM3-AVNs indicate that periods of confined motion are interrupted by relatively short periods of directed motion with $S_{MSS} > 0.5$. The latter are responsible for achieving a segregation of initially randomly distributed AVNs into larger clusters.

The average and maximum speeds for the recorded trajectories are graphed in Figure 4d and e, respectively. The average speed for all trajectories is 0.16 ± 0.11 μm/s, and more than 70% of the AVNs achieve maximum speeds of <0.5 μm/s. Although a few AVNs (e.g., AVN1 in Figure 4b) show a faster directed motion, indicative of a microtubule-dependent molecular motor driven process, the motion pattern of the AVN majority is compatible with processive, actin-based myosin motors, which achieve speeds between 0.1 and 0.5 μm/s in vivo.[42] The measured AVN speed distribution and the observation that a perturbation of the cortical actin network (de)polymerization inhibits AVN clustering (Figure 3c) are, in principle, consistent with a role of the actin-binding myosin in the observed AVN translocation. CD169 is, however, a transmembrane protein with a very short cytoplasmic tail,[24] and it is unclear whether it can directly bind to myosin motor proteins associated with the cortical actin network. Another possible explanation of the observed motion pattern, which does not require direct interactions between CD169 and motor proteins, is based on a concerted restructuring of the cortical actin network to guide the diffusion of CD169. According to this model, CD169 transmembrane proteins are confined to cortical actin defined membrane compartments (corrals).[43] Binding of GM3-displaying AVNs or virus particles either induces a directed restructuring of the cortical actin network in the vicinity of the receptor or makes the network permissible in one specific direction. The CD169 receptors present in a cortical actin confined membrane microdomain explore the accessible space through diffusion and, thus, follow the trajectory defined by the dynamic cortical actin network.

Independent of the exact mechanism of AVN translocation, our studies show clearly that GM3-CD169 binding is sufficient to initiate a coordinated transport of GM3-AVN-bound CD169 receptors over relatively large cellular distances. Considering that CD169 is a transmembrane protein without known transduction motifs,[44] it remains unclear how nanoconjugated CD169 can induce this cell-wide response. We postulate that the receptor initiates the observed cellular response by recruiting one or more yet to be identified cofactor(s). A future identification of these cofactors not only would result in an improved understanding of the HIV-1 trans-infection mechanism, but might also identify a potential pathway for a general intracellular NP delivery into nonlysosomal, nondegradative compartments.
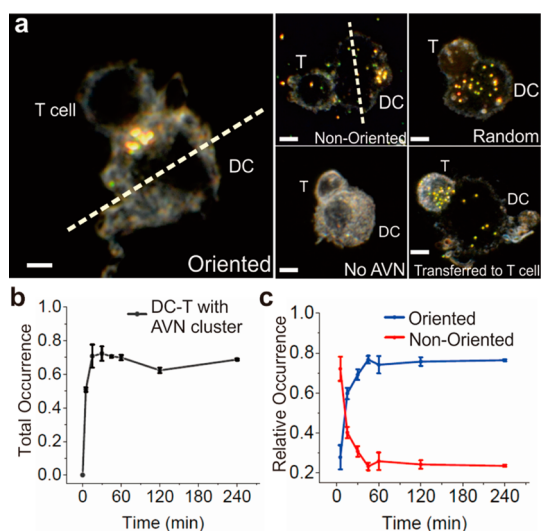
Figure 5. Classification of mDC–T cell conjugates with GM3-AVN clusters. (a) Examples of *Oriented*, *Nonoriented*, *Random*, and *No AVN* spatial distribution patterns. The classification is determined by the relative orientation of the AVN cluster and T cell (see text). In the case of the *Oriented* pattern the AVN cluster is located in the same cell hemisphere as the T cell, whereas for the *Nonoriented* pattern, T cell and AVN cluster are located in two different hemispheres of the mDC, as indicated by the dashed lines. Scale bars = 1 μm. (b) Total occurrence (±SD) of mDC–T conjugates containing GM3-AVN clusters as a function of time. (c) Relative fraction (±SD) of *Oriented* and *Nonoriented* patterns as a function of time. Data were collected from two donors in two independent experiments. More than 200 conjugates were counted for each time point. Error bars are standard deviations.

AVN Polarization in mDC–T Cell Contacts. To determine if GM3-AVNs successfully access trafficking mechanisms that have previously been shown to lead to an accumulation of HIV-1 particles at the mDC–T cell synapse,[10,11] we probed the fate of GM3-AVN clusters in mDCs upon initiation of mDC–CD4$^+$ T cell conjugates. Mature DCs were pretreated with GM3-AVNs for 1.5 h to ensure completion of AVN cluster formation before CD4$^+$ T cells were added (1:1 mDC/T cell ratio). The cells were then incubated for 5–240 min before they were inspected in the dark-field microscope to classify the formed mDC–T cell conjugates. We differentiated five classes of mDC–T cell conjugates as shown in Figure 5a. Our categorization was based on the orientation of the AVNs with regard to the T cell and followed previous strategies[45] for quantifying the localization of HIV-1 particles at the mDC–T cell synaptic junction. Depending on the relative location of the AVN cluster and T cell, we refer to the mDC–T cell conjugates as *Oriented* (AVN cluster is located in the same hemisphere of the mDC as the T cell) and *Nonoriented* (AVN cluster is localized in the opposite hemisphere of the mDC as the T cell). Other classifications included *No AVN*, *Random* (bound AVNs are not clustered), or *Transferred to T cell*, but these phenotypes were less frequent (Figure S4) and play only a secondary role. To avoid any ambiguity in the analysis, we restricted our analysis to mDC–T cell conjugates with at most two T cells per mDC. For those conjugates with two T cells, the mDC was segmented such that one hemisphere contained both T cells (Figure S5).

The fraction of mDCs that exhibit AVN segregation and that have at least one T cell bound increases quickly to approximately 71% of the entire ensemble within the first 15 min after addition of T cells but remains almost constant for longer incubation times (Figure 5b). In the next step, we subdivided these mDC–T cell conjugates into the *Oriented* and *Nonoriented* subgroups. The results of this classification for approximately 200 mDCs for each time point derived from two different donors are summarized in Figure 5c. The *Oriented* pattern shows a continuous increase within the first 60 min, while the *Nonoriented* pattern decreases (Figure 5c). The *Oriented/Nonoriented* ratio changes from 1:1 to 3:1 within the first 60 min and remains approximately constant for longer incubation times.

To further characterize the mDC–T cell interface in the case of the *Oriented* phenotype, we performed immunofluorescence studies and evaluated the colocalization between AVN clusters and known markers of virological synapses at the mDC–T cell contact after 2 h of co-incubation. CD169 has been demonstrated to induce HIV-1 trafficking to the infectious synapse upon T cell contact and to show a strong polarized distribution toward the mDC–T cell interface.[10,13] Likewise, the tetraspanin CD81 is also enriched at the mDC–T cell virological synapse.[46,47] Finally, the restructuring of the cell membranes at an infectious synapse requires actin, and high local F-actin concentrations have been shown to colocalize with the site of HIV-1 particle accumulation at the virological synapse.[48] Figure 6 shows correlated dark-field/fluorescence images of mDC–T cell conjugates with an *Oriented* GM3-AVN distribution stained for CD169 (a), CD81 (b), and F-actin (c). All of these markers colocalize with the GM3-AVN cluster at the mDC–T cell synapse, confirming an mDC–T cell interface that shares significant morphological and functional similarities with HIV-1-induced virological synapses.

Mechanisms of GM3-AVN Enrichment at the Virological Synapse. The anticorrelated changes in the occurrence of *Oriented* and *Nonoriented* mDC–T cell conjugates within the first 60 min of observation (Figure 5c) imply a conversion of the *Nonoriented* into the *Oriented* pattern as a consequence of some relative motion of AVN clusters and T cells toward each other. To test this hypothesis, we continuously imaged mDC–T cell conjugates as a function of time and monitored the relative alignment of the AVN cluster and T cell. In these experiments mDCs pulsed with GM3-AVNs were immobilized on polylysine-treated glass-bottom dishes. AVN cluster-containing mDCs were located in the dark-field microscope equipped with a cage incubator and centered in the field of view. CD4$^+$ T cells prestained with

CellTracker Orange were subsequently locally delivered with a micropipette mounted on a micromanipulator. The T cells bound efficiently to the mDCs upon contact formation, and a binding event defined the starting point for the optical tracking. Our optical setup allowed the acquisition of both fluorescence and elastic scattering images, ensuring a precise localization of both fluorescently marked T cells and AVN clusters.

The live-cell imaging studies revealed two different relative motion patterns between AVN clusters and T cells. The most commonly observed motion is illustrated in Figure 7a. The series of images of a mDC−T cell conjugate with an AVN cluster recorded at different time points shows a rapid motion ("rolling") of the T cell across the mDC surface within the first 10 min that leads the T cell into the vicinity of the AVN cluster (green arrow). Interestingly, the T cell motion stops

almost entirely once the cell has reached the vicinity of the AVN cluster. We continued to image the mDC−T cell conjugate for another 20 min and did not observe any further movement of the T cell. Overall, the movement of the T cell along the mDC surface converts the AVN pattern from the *Nonoriented* into the *Oriented* form in the course of approximately 10 min. We observed similar T cell rolling behaviors that eventually resulted in an immobilization of the T cell in the vicinity of an AVN cluster for six different mDC−T cell conjugates in three independent experiments. The observed T cell behavior is consistent with the known rapid scanning of T cells over DC surfaces to identify cognate peptide−MHC complexes prior to prolonged arrest and forming stable mDC−T cell synapses.[49−51] Our T cell tracking data suggest that peripheral compartments containing GM3-AVNs in mDCs might be segregated with unique surface features that trigger arrest of scanning T cells and initiate, thus, the formation of a stable synaptic contact.

Figure 7b illustrates a second pattern of observed mDC−T cell motility. Here, the T cells in contact with the mDC do not systematically scan over the cell surface but, instead, remain located close to their original binding sites. Interestingly, in this case of immobilized T cells the AVN cluster (green arrow) migrates toward one of the bound T cells and reaches the mDC−T cell contact area within 30 min. The observed average speed for the AVN cluster displacement is ∼100 nm/min, which is distinctly slower than what was observed for the individual GM3-AVNs in Figure 4d. The direct motion of the AVN cluster was much less frequent than the T cell scanning of Figure 7a, and we cannot exclude that the immobilization of the T cells was a consequence of their binding to the glass bottom of the dish. Future tracking studies in free-floating mDC−T cell conjugates will be able to determine the relevance of this second motion pattern.

SUMMARY AND CONCLUSION

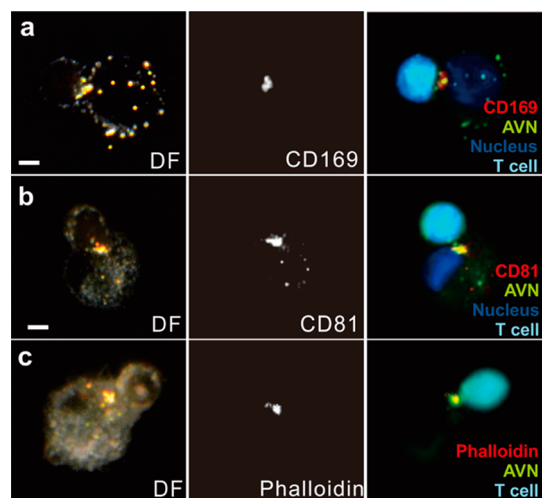The systematic AVN imaging studies performed in this work suggest the mechanistic model summarized

Figure 6. Characterization of *Oriented* mDC−T cell conjugates through correlated dark-field/fluorescence imaging. The cells were stained for CD169 (a), CD81 (b), and F-actin (c). The left row shows the dark-field color image, the middle row the monochromatic fluorescence image, and the right row a false-color overlay. Colocalization is indicated in yellow (AVN = green, fluorescence marker = red). T cells were stained with CellTracker Orange and are plotted in cyan pseudocolor. Nuclei were stained with DAPI fluorescence stain and are marked blue. Scale bars = 1 μm.
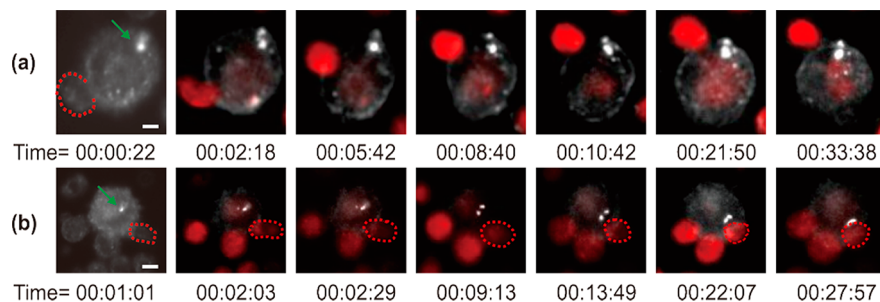
Figure 7. Real-time monitoring of the *Oriented* mDC−T cell pattern formation. (a) Snapshots of selected time points showing a T cell rolling across the mDC surface toward the GM3-AVN cluster (bright white dot marked by green arrow). (b) Snapshots of selected time points showing AVN cluster migrating toward T cell. Scale bars = 1 μm. The images show dark-field images with superimposed fluorescence image of the labeled T cells. Fluorescence images only served the purpose of identifying the T cells and were not recorded for all frames.
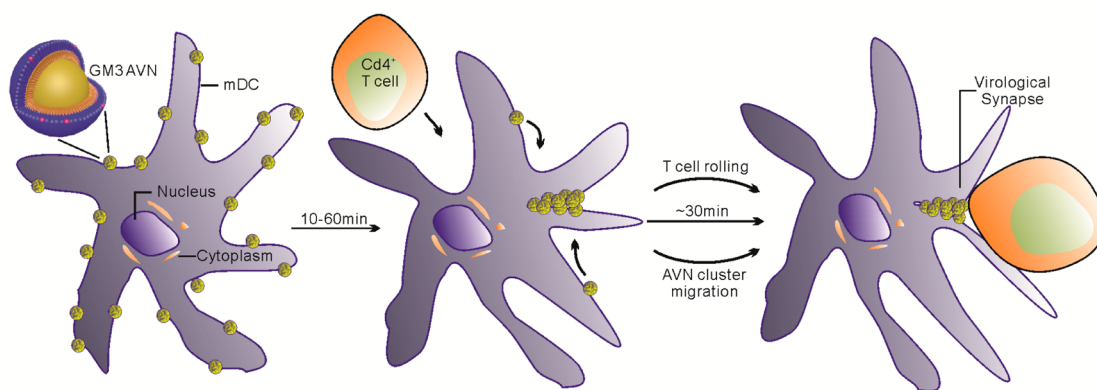
Figure 8. Model of AVN concentration at mDC–T cell virological synapse consistent with the experimental observations. GM3-presenting AVNs are segregated in peripheral membrane compartments that attract surface scanning T cells. The T cell binding induces the formation of a virological synapse.

in Figure 8 for the observed AVN concentration at the virological synapse. AVNs bind to mDCs and induce the formation of peripheral AVN clusters. These AVN-enriched compartments are then detected by surface scanning T cells, which bind at or close to this site and initiate the formation of a virological synapse at the site of the AVN clustering. According to this model GM3-presenting AVNs recapitulate key steps of the HIV-1 trans-infection mechanism in mDCs. In particular, we have shown that the inclusion of GM3 in a self-assembled membrane around a gold NP suffices to achieve an efficient and selective binding to mDCs and to subsequently induce a segregation of the GM3-NPs in tetraspanin $CD81^+$ and $CD169^+$ nonlysosomal compartments within 10–60 min post NP challenge. The observation that GM3-AVN segregation requires an intact dynamic cortical F-actin network but is not affected by microtubule disruption through colchicine indicates an F-actin-dependent AVN segregation mechanism. The optical tracking of T cells on GM3-AVN-containing mDCs has shown that the formation of GM3-AVN-enriched compartments impacts mDC–T cell behavior. Most importantly, addition of $CD4^+$ T cells to mDCs with preformed GM3-AVN clusters was observed to frequently result in the arrest of mDC surface scanning T cells in the vicinity of a GM3-AVN cluster. In contrast, trafficking of GM3-AVN clusters toward immobilized T cells occurred with much lower frequency. The mDC–T cell synaptic junctions containing GM3-AVN clusters are enriched in CD169, CD81, and F-actin and, thus, show a remarkable resemblance

to previously described HIV-1-containing mDC–T cell virological synapses.[10,11,27,46,52] While the enrichment of AVNs at the mDC–T cell interface was observed frequently, an actual transfer of AVNs from mDC to T cell was rare (less than 5% of the total AVN-containing mDC–T conjugates; see Figure S4) under our experimental conditions, even after prolonged coculturing of mDCs and T cells. This finding indicates that while GM3 is sufficient to induce the formation of an mDC–T cell virological synapse, additional factors besides GM3, such as engagement of CD4 on the T cell surface by the virus glycoprotein, gp120, might be required to achieve an efficient transfer of AVNs to T cells. To this end, insertion of T cell-derived filopodia into mDC invaginations harboring HIV-1 particles has been suggested to initiate directed release of mDC-bound virus particles toward the T cell surface.[48]

Despite these limitations with regard to AVN transfer from mDC to T cell, the demonstrated ability to achieve an efficient localization at the mDC–T cell synaptic junction and to trigger the enrichment of virological synapse characteristic molecular functionalities proves the capacity of GM3-AVNs to target key events in the adaptive immune response. GM3-AVNs are, therefore, promising functional NPs with tangible translational potential for enhanced immunization and therapeutic strategies. This work also underlines the value of self-assembled AVNs with defined composition as biophysical nanotools to study lipid-based intercell signaling and self-recognition mechanisms and their parasitization through enveloped viruses.

METHODS AND MATERIALS

AVN Preparation. Membrane-wrapped nanoparticles were generated by co-incubating citrate-stabilized gold nanoparticles with octadecanethiol in the presence of a liposome with defined lipid composition that act as a lipid reservoir. A total of 1 μmol of lipid mixture (Table S1) was dissolved in 100 μL of chloroform, rotary evaporated dried to form a thin layer on a 25 mL round-bottom flask, and further dehydrated under

vacuum overnight. A 1 mL amount of 20 mM HEPES buffer (pH 7.2) was then added under argon to the lipid dry layer and vigorously agitated to form a cloudy solution. The solution was subsequently sonicated with a probe sonicator (Fisher Scientific model 120 Sonic Dismembrator, 50/60 Hz) for 2.5 min or until the solution became clear. The formed liposome solution could be stored at 4 °C under argon until further use. A 1 mL sample of 1.1×10^{10} particles mL^{-1} 80 nm gold NPs was pelleted by

centrifugation at 600g. The pellet was then added into 0.5 mL of the prepared liposome solution and filled to 1 mL with 20 mM HEPES buffer. A 200 μL portion of 0.01 mg mL^{-1} 1-octadeca-nethiol (in ethanol) was added to the solution and agitated overnight to ensure thorough mixing and reaction. AVNs were washed by repeated centrifugation and resuspension (3 times, 600g) in DDI water and finally resuspended into 100 μL of 20 mM HEPES buffer.

AVN Characterization. The hydrodynamic radius and zeta potential were obtained from 1 $\times$ 10^7 particles mL^{-1} containing AVN dispersions in 10 mM NaCl (pH 7.0) using a Zetasizer Nano ZS90 (Malvern, Worcestershire, UK). The absorption spectra were acquired on an Agilent Cary 5000 UV/vis spectrometer. Base line correction was performed with a 10 mM NaCl solution. AVN concentrations were calculated from the recorded spectra according to Lambert–Beer's law (ε = 9.124 $\times$ 10^{10} M^{-1} cm^{-1}). AVNs containing Topfluor-labeled cholesterol (Avanti Lipids) were then drop-cast onto glass coverslips to validate successful membrane assembly by colocalizing membrane fluorescence and NP scattering signals. To prepare samples for inspection in the TEM, the AVN solution was diluted to 1 $\times$ 10^7 particles mL^{-1} with DDI water and drop-cast onto carbon-coated TEM grids. Excess solution was removed by a clean filter paper after 1 min incubation, and the samples were dried and stored under vacuum before imaging using a JEOL JEM 2010 HRTEM with a 200 kV acceleration voltage.

ICP-MS Quantification of AVN-mDC Binding. A total of 1 $\times$ 10^7, 1 $\times$ 10^8, and 1 $\times$ 10^9 AVNs containing no GM3 or GalCer, 3% GalCer, or 3% GM3 were added to 3 $\times$ 10^5 mDCs and incubated in 100 μL serum-free growth medium (Roswell Park Memorial Institute Medium, RPMI-1640) at 37 °C, 5% CO$_2$ for 5 min. Free, unbound AVNs were then removed by centrifugation at 270g for 5 min. The cells were subsequently fixed with 4% parafor-maldehyde and dialyzed with 1$\times$ PBS buffer (pH = 7.0) over-night. After collection through centrifugation, the cells were counted. The cells were dissolved in aqua regia, and the concentration of gold in the samples was quantified with a Thermo (VG) PlasmaQuad (PQ) ExCell inductively coupled plas-ma mass spectrometer.

Flow Cytometry Quantification of AVN-mDC Binding. All AVNs contained 0.5% TopFluor PC (Avanti). Total amounts of 1 $\times$10^7, 3 $\times$ 10^7, and 1 $\times$ 10^8 AVNs with 3% GM3 or GalCer or without any glycosphingolipids (blank) were added to 3 $\times$ 10^5 mDCs and incubated in 100 μL of serum-free growth medium (RPMI-1640) at 37 °C, 5% CO$_2$ for 15 or 30 min. Free, unbound AVNs were then removed by centrifugation at 270g for 5 min. The cells were subsequently fixed with 4% paraformaldehyde for 15 min at room temperature. The fluorescence intensity distribution for each sample was tested with a BD LSRII instrument and analyzed through FlowJo software.

Fluorescence Staining of AV- Loaded mDCs and mDC–T Cell Conjugates. In a typical experiment 3 $\times$ 10^5 mDCs were incubated in 100 μL of serum-free RPMI-1640 with 1 $\times$ 10^8 GM3-AVNs for defined times. AVNs were then removed by centrifugation (270g) and resuspended in serum-free RPMI. For some experiments, Lyso-Tracker DeepRed (Invitrogen) (final concentration of 100 nM) and Hoechst 33342 were added, and cells were incubated for 30 min at 37 °C to stain the lysosome and nucleus, respectively. The cells were then washed by centrifugation and fixed with 4% paraformaldehyde (10 min, room temperature). To stain CD81 or CD169, mDCs were first fixed with 4% parafomaldehyde and then permeabilized with 0.5% Triton X100, blocked with 20% normal human serum (NHS). For CD81 staining, α-CD81 mAb (BD; 1:50 dilution) and Alexa488 conjugated secondary anti-body (Invitrogen; 1:50 dilution) were added successively. For CD169 staining, Alexa647-conjugated α-CD169 mAb (Bio-legend; 1:50 dilution) was used. To stain for F-actin, paraformal-dehyde-fixed mDCs were treated with fluorescein phalloidin (Life Technologies, 1:40 dilution) following the manufacture's protocol. To stain mDC–T cell conjugates, the staining pro-cedures were identical with the exception that AVN-treated mDCs were incubated with CD4$^+$ T cells in 1:1 ratio at 37 °C for 2 h in serum-free RPMI-1640 prior to any staining procedure.

Statistical Analysis of AVN Clustering and mDC–T Cell Conjugate Formation. For AVN cluster formation, 1 $\times$ 10^8 GM3-containing

AVNs were added to 3 $\times$ 10^5 DCs and incubated in 100 μL of serum-free RPMI-1640 at 37 °C for 5, 10, 20, 30, 45, and 60 min. Free, unbound AVNs were then removed by gentle washing through centrifugation and resuspension (2$\times$) and fixed in 4% paraformaldehyde. The cells were then cytospun onto glass coverslips (24 mm $\times$ 60 mm) and inspected in the dark-field microscope. For mDC–T cell conjugates, 1 $\times$ 10^8 GM3-contain-ing AVNs were added to 3 $\times$ 10^5 DCs and incubated at 37 °C for 1.5 h in 100 μL of serum-free RPMI-1640, before the DCs were collected through centrifugation at 270g to purify from free unbound AVNs. The DCs were then mixed with CD4$^+$ T cells in a 1:1 ratio and incubated in serum-free RPMI-1640 at 37 °C for 5, 15, 30, 45, 60, 120, and 240 min, respectively. The cells were then fixed with 4% paraformaldehyde and cytospun onto glass coverslips for further imaging and counting. Counts of DCs and conjugates were collected from recorded movies across the entire imaging area, to ensure the randomness and fairness for the sample set. Data were collected from three different donors in three independent experiments (n = 3), and more than 200 mDCs were counted for each time point.

Image Acquisition and Processing. Optical imaging was per-formed with a modified Olympus IX71 inverted microscope (Figure S6) equipped with a cage incubator system. Dark-field scattering images were illuminated with a 100 W tungsten lamp through a high-NA oil dark-field condenser (NA = 1.2–1.4) and were collected with a 60$\times$ oil objective with adjustable NA (NA = 0.65–1.25). Color dark-field images and movies were recorded with a Nikon D3100 SLR through an eyepiece adapter. Monochromatic dark-field images and movies were recorded with an Andor Ixon electron multiplying charge coupled device detector. Fluorescence imaging was performed under epi-illumination using appropriate filter sets. Images were aligned and superimposed using ImageJ. Particle trajectories were recorded as short movies, and MSS slopes and particle speeds were analyzed with home-written MATLAB codes.[53]

Imaging AVN Clustering. A total of 1 $\times$10^8 GM3-containing AVNs were mixed with 3 $\times$ 10^5 DCs in 100 μL of serum-free growth medium at 4 °C for 10 min; unbound AVNs were removed by washing through centrifugation and resuspension. The DCs were then placed into polylysine-treated round glass-bottom dishes. CO$_2$-independent medium (Life Technologies) was added after the cells sedimented to the bottom, to ensure adequate environmental conditions for live cell imaging stud-ies. The cells were then transferred into the microscope at 37 °C, and data acquisition was initiated.

Tracking the Relative Motion of AVN Clusters and T Cells. A total of 3 $\times$ 10^5 DCs were pretreated with 1 $\times$ 10^8 GM3-containing AVNs for 1.5 h at 37 °C in 100 μL of serum-free growth medium and washed by centrifugation (270g) and resuspension. T cells were stained with CellTracker Orange for 30 min at 37 °C and washed to remove the free dye. In the microscope incubator, the DCs were dropped onto polylysine-pretreated round glass-bottom dishes and incubated at 37 °C for 5 min. Candidate mDCs containing a peripheral AVN cluster were then located under dark-field illumination. A stream of T cells was locally adminis-tered using a micromanipulator equipped with a micropipette. The interactions of T cells with mDCs were continuously tracked under dark-field illumination, and fluorescence images were recorded at selected time points.

SEM Sample Preparation and Imaging. A total of 5.6 $\times$ 10^6 mDCs were incubated with 5.6 $\times$ 10^9 GM3-containing AVN2 for 1 h at 37 °C. Cells were washed twice with PBS and fixed with 4% PFA and 1% glutaraldehyde in 0.1 M PHEM buffer (60 mM PIPES, 25 mM HEPES, 2 mM MgCl$_2$, and 10 mM EGTA). Cells were further fixed with 2% osmium tetroxide, dehydrated in ethanol, and embedded in epoxy resin.[54] Semithin sections (0.8 μm) of embedded cells were stained with 1% toluidine blue and inspected by light microscopy to verify the presence of suffi-cient cells. Cell sections of approximately 1 μm thickness were dried on a glass coverslip that was attached to a SEM sample holder (stub) with double-sided copper tape. The samples were then coated with a layer of carbon (50–80 nm) in a DV-502 high-vacuum evaporator (Denton Vacuum, Cherry Hill, NJ, USA). A strip of PELCO colloidal graphite (Ted Pella, Redding, CA, USA) connected the glass coverslip to a metal stub for grounding.

The SEM sample was then imaged with a Zeiss Supra 55VP field emission scanning electron microscope at an acceleration voltage of 2−5 kV and elementarily analyzed by the energy dispersive X-ray spectroscopy module contained in the SEM.

Virus-like Particles. HIV Gag-eGFP VLPs were generated as previously described,[12] by transient transfection (calcium phosphate mediated) of HEK293T cells with a pGag−eGFP expression plasmid. VLPs were collected 2 days post-transfection, purified from cell debris by filtering through 450 nm pore size filters, and stored at −80 °C prior to use.

Dendritic Cells and T Cells. Primary monocyte-derived DCs were differentiated from CD14$^+$ peripheral blood monocytes and matured with LPS (100 ng mL^{-1}) for 2 days prior to use.[10] Primary human CD4$^+$ T cells were positively isolated from CD14-depleted peripheral blood mononuclear cells using CD4-conjugated magnetic beads and LS MACS cell separation columns (Miltenyi Biotech). Positively isolated CD4$^+$ T cells were activated with 2% PHA (Invitrogen) for 2 days, washed, and cultured in IL-2 (50 U/mL) containing RPMI supplemented with 10% FBS.

REFERENCES AND NOTES

1. Grakoui, A.; Bromley, S. K.; Sumen, C.; Davis, M. M.; Shaw, A. S.; Allen, P. M.; Dustin, M. L. The Immunological Synapse: A Molecular Machine Controlling T Cell Activation. *Science* **1999**, *285*, 221–227.
2. Chmielowski, B.; Ribas, A. *Targeting Immunological Synapse: New Horizons in Immunotherapy for Cancer*; Humana Press, 2009.
3. Wiendl, H.; Hohlfeld, R. *Immune Regulation and Immunotherapy in Autoimmune Disease*; Springer, 2007.
4. Jolly, C.; Kashefi, M.; Hollinshead, M.; Sattentau, Q. J. HIV-1 Cell to Cell Transfer Across an Env-Induced, Actin-Dependent Synapse. *J. Exp. Med.* **2004**, *199*, 283–293.
5. Hubner, W.; McNerney, G. P.; Chen, P.; Dale, B. M.; Gordon, R. E.; Chuang, F. Y.; Li, X. D.; Asmuth, D. M.; Huser, T.; Chen, B. K. Quantitative 3D Video Microscopy of HIV Transfer across T Cell Virological Synapses. *Science* **2009**, *323*, 1743–1747.
6. Vasiliver-Shamis, G.; Dustin, M. L.; Hioe, C. E. HIV-1 Virological Synapse Is Not Simply a Copycat of the Immunological Synapse. *Viruses* **2010**, *2*, 1239–1260.
7. Macdonald, D.; Wu, L.; Bohks, S. M.; Kewal Ramani, V. N.; Unutmaz, D.; Hope, T. J. Recruitment of HIV and Its Receptors to Dendritic Cell-Tcell Junctions. *Science* **2003**, *300*, 1295–1297.
8. Jolly, C.; Sattentau, Q. J. Retroviral Spread by Induction of Virological Synapses. *Traffic* **2004**, *5*, 643–650.
9. Haase, A. T. Population Biology of HIV-1 Infection: Viral and CD4+ T Cell Demographics and Dynamics in Lymphatic Tissue. *Annu. Rev. Immunol.* **1999**, *17*, 625–656.
10. Puryear, W. B.; Akiyama, H.; Geer, S. D.; Ramirez, N. P.; Yu, X.; Reinhard, B. M.; Gummuluru, S. Interferon-Inducible Mechanism of Dendritic Cell-Mediated HIV-1 Dissemination is Dependent on the Siglec, CD169. *PLoS Pathog.* **2013**, *9*, e1003291.
11. Izquierdo-Useros, N.; Lorizate, M.; Contreras, F.-X.; Rodriguez-Plata, M. T.; Glass, B.; Erkizia, I.; Prado, J. G.; Casas, J.; Fabrias, G.; Krausslich, H. G.; *et al.* Sialyllactose in Viral Membrane Gangliosides Is a Novel Molecular Recognition Pattern for Mature Dendritic Cell Capture of HIV-1. *PLoS Biol.* **2012**, *10*, e1001315.
12. Puryear, W. B.; Yu, X.; Ramirez, N. P.; Reinhard, B. M.; Gummuluru, S. HIV-1 Incorporation of Host-Cell-Derived Glycosphingolipid GM3 Allows for Capture by Mature Dendritic Cells. *Proc. Natl. Acad. Sci. U.S.A.* **2012**, *109*, 7475–7480.
13. Izquierdo-Useros, N.; Lorizate, M.; Puertas, M. C.; Rodriguez-Plata, M. T.; Zangger, N.; Erikson, E.; Pino, M.; Erkizia, I.; Glass, B.; Clotet, B.; Keppler, O. T.; Telenti, A.; Krausslich, H. G.; Martinez-Picado, J.; *et al.* Siglec-1 Is a Novel Dendritic Cell Receptor That Mediates HIV-1 Trans-Infection through Recognition of Viral Membrane Gangliosides. *PLoS Biol.* **2012**, *10*, e1001448.
14. Yameen, B.; Choi, W. I.; Vilos, C.; Swami, A.; Shi, J.; Farokhzad, O. C. Insight into Nanoparticle Cellular Uptake and Intracellular Targeting. *J. Controlled Release* **2014**, *190*, 485–499.
15. Niu, Y.; Yu, M.; Hartono, S. B.; Yang, J.; Xu, H.; Zhang, H.; Zhang, J.; Zou, J.; Dexter, A.; Gu, W.; *et al.* Nanoparticles Mimicking Viral Surface Topography for Enhanced Cellular Delivery. *Adv. Mater.* **2013**, *25*, 6233–6237.
16. Aoyama, Y.; Kanamori, T.; Nakai, T.; Sasaki, T.; Horiuchi, S.; Sando, S.; Niidome, T. Artificial Viruses and Their Application to Gene Delivery. Size-Controlled Gene Coating with Glycocluster Nanoparticles. *J. Am. Chem. Soc.* **2003**, *125*, 3455–3457.
17. Mastrobattista, E.; van der Aa, A. E. M.; Hennink, W. E.; Crommelin, D. J. A. Artificial Viruses: A Nanotechnological Approach to Gene Delivery. *Nat. Rev. Drug Discovery* **2006**, *5*, 115–121.
18. van Schooneveld, M. M.; Vucic, E.; Koole, R.; Zhou, Y.; Stocks, J.; Cormode, D. P.; Tang, C. Y.; Gordon, R. E.; Nicolay, K.; Meijerink, A.; *et al.* Improved Biocompatibility and Pharmacokinetics of Silica Nanoparticles by Means of a Lipid Coating: A Multimodality Investigation. *Nano Lett.* **2008**, *8*, 2517–1525.
19. Allijin, I. E.; Leong, W.; Tang, J.; Gianella, A.; Mieszawska, A. J.; Fay, F. S.; Ma, G.; Russel, S.; Callo, C. B.; Gordon, R. E.; *et al.* Gold Nanocrystal Labeling Allows Low-Density Lipoprotein Imaging from the SubCellular to Macroscopic Level. *ACS Nano* **2013**, *7*, 9761–9770.
20. Thaxton, C. S.; Daniel, W. L.; Gilijohann, D. A.; Thomas, A. D.; Mirkin, C. A. Templated Spherical High Density Lipoprotein Nanoparticles. *J. Am. Chem. Soc.* **2009**, *131*, 1384–1385.
21. Ashley, C. E.; Carnes, E. C.; Phillips, G. K.; Padilla, D.; Durfee, P. N.; Brown, P. A.; Hanna, T. N.; Liu, J.; Phillips, B.; Carter, M. B.; *et al.* The Targeted Delivery of Multicomponent Cargos to Cancer Cells by Nanoporous Particle-Supported Lipid Bilayers. *Nat. Mater.* **2011**, *10*, 389–397.
22. Yang, J. A.; Murphy, C. J. Evidence for Patchy Lipid Layers on Gold Nanoparticle Surfaces. *Langmuir* **2012**, *28*, 5404–5416.
23. Yu, X.; Feizpour, A.; Ramirez, N.-G. P.; Wu, L.; Akiyama, H.; Gummuluru, S.; Reinhard, B. M. Glycosphingolipid-Functionalized Nanoparticles Recapitulate CD169-dependent HIV-1 Uptake and Trafficking in Dendritic Cells. *Nat. Commun.* **2014**, *5*, 4136.
24. Hartnell, A.; Steel, J.; Turley, H.; Jones, M.; Jackson, D. G.; Crocker, P. R. Characterization of Human Sialoadhesin, a Sialic Acid Binding Receptor Expressed by Resident and Inflammatory Macrophage Populations. *Blood* **2001**, *97*, 288–298.
25. Chan, R.; Uchil, P. D.; Jin, J.; Shui, G.; Ott, D. E.; Mothes, W.; Wenk, M. R. Retroviruses Human Immunodeficiency Virus and Murin Leukemia Virus Are Enriched in Phosphoinositides. *J. Virol.* **2008**, *82*, 11228–11238.
26. Brugger, B.; Glass, B.; Haberkant, P.; Leibrecht, I.; Wieland, F. T.; Kräusslich, H.-G. The HIV Lipidome: A Raft with an Unusual Composition. *Proc. Natl. Acad. Sci. U.S.A.* **2006**, *103*, 2641–2646.
27. Akiyama, H.; Ramirez, N. G.; Gudheti, M. V.; Gummuluru, S. CD169-Mediated Trafficking of HIV to Plasma Membrane Invaginations in Dendritic Cells Attenuates Efficacy of Anti-gp120 Broadly Neutralizing Antibodies. *PLoS Pathog.* **2015**, *11*, e1004751.

28. Izquierdo-Useros, N.; Lorizate, M.; McLaren, P. J.; Telenti, A.; Krausslich, H. G.; Martinez-Picado, J. HIV-1 Capture and Transmission by Dendritic Cells: The Role of Viral Glycolipids and the Cellular Receptor Siglec-1. *PLoS Pathog.* **2014**, *10*, e1004146.

29. Gummuluru, S.; Ramirez, N.-G. P.; Akiyama, H. CD169-Dependent Cell Associated HIV-1 Transmission: A Driver of Virus Dissemination. *J. Infect. Dis.* **2013**, *210* (Suppl. 3), S641–S647.

30. Kreibig, U.; Vollmer, M. *Optical Properties of Metal Clusters*; Springer: Berlin, 1995.

31. Wu, L.; Reinhard, B. M. Probing Subdiffraction Limit Separations with Plasmon Coupling Microscopy: Concepts and Applications. *Chem. Soc. Rev.* **2014**, 3884–3897.

32. Sonnichsen, C.; Franzl, T.; Wilk, T.; von Plessen, G.; Feldmann, J. Plasmon Resonances in Large Noble-Metal Clusters. *New J. Phys.* **2002**, *4*, 93.1–93.8.

33. Lakadamyali, M.; Rust, M. J.; Babcock, H. P.; Zhuang, X. W. Visualizing Infection of Individual Influenza Viruses. *Proc. Natl. Acad. Sci. U.S.A.* **2003**, *100* (16), 9280–9285.

34. Brandenburg, B.; Zhuang, X. W. Virus Trafficking - Learning from Single-Virus Tracking. *Nat. Rev. Microbiol.* **2007**, *5* (3), 197–208.

35. Ewers, H.; Smith, A. E.; Sbalzarini, I. F.; Lilie, H.; Koumoutsakos, P.; Helenius, A. Single-Particle Tracking of Murine Polyoma Virus-like Particles on Live Cells and Artificial Membranes. *Proc. Natl. Acad. Sci. U.S.A.* **2005**, *102* (42), 15110–15115.

36. Burckhardt, C. J.; Somalainen, M.; Schoenenberger, P.; Boucke, K.; Hemmi, S.; Greber, U. F. Drifting Motions of the Adenovirus Receptor CAR and Immobile Integrins Initiate Virus Uncoating and Membrane Lyctic Protein Exposure. *Cell Host Microbe* **2011**, *10*, 105–117.

37. Sherer, N. M.; Lehmann, M. J.; Jimenez-Soto, L. F.; Horensavitz, C.; Pypaert, M.; Mothes, W. Retroviruses Can Establish Filopodial Bridges for Efficient Cell-to-Cell Transmission. *Nat. Cell Biol.* **2007**, *9*, 310–315.

38. Ferrari, R.; Manfroi, A. J.; Young, W. R. Strongly and Weakly Self-Similar Diffusion. *Phys. D (Amsterdam, Neth.)* **2001**, *154*, 111–137.

39. Sbalzarini, I. F.; Koumoutsakos, P. Feature Point Tracking and Trajectory Analysis for Video Imaging in Cell Biology. *J. Struct. Biol.* **2005**, *151*, 182–195.

40. Schelhaas, M.; Ewers, H.; Rajamaeki, M. L.; Day, P. M.; Schiller, J. T.; Helenius, A. Human Papillomavirus Type 16 Entry: Retrograde Cell Surface Transport along Actin Rich Protrusions. *PLoS Pathog.* **2008**, *4*, e1000148.

41. Chen, T.; Reinhard, B. M. Characterizing the Lateral Friction of Nanoparticles on on-Chip Integrated Black Lipid Membranes. *Small* **2013**, *9*, 876–884.

42. Vaughan, J. C.; Brandenburg, B.; Hogle, J. M.; Zhuang, X. Rapid Actin-Dependent Viral Motility in Live Cells. *Biophys. J.* **2009**, *97*, 1647–1656.

43. Kusumi, A.; Nakada, C.; Ritchie, K.; Murase, K.; Suzuki, K.; Murakoshi, H.; Kasai, R. S.; Kondo, J.; Fujiwara, T. Paradigm Shift of the Plasma Membrane Concept from the Two-Dimensional Continuum Fluid to the Partitioned Fluid: High-Speed Single-Molecule Tracking of Membrane Molecules. *Annu. Rev. Biophys. Biomol. Struct.* **2005**, *34*, 351–378.

44. Saunderson, S. C.; Dunn, A. C.; Crocker, P. R.; McLellan, A. D. CD169 Mediates the Capture of Exosomes in Spleen and Lymph Node. *Blood* **2014**, *123*, 208–216.

45. Wang, J.-H.; Wells, C.; Wu, L. Macropinocytosis and Cytoskeleton Contribute to Dendritic-Mediated HIV-1 Transmission to CD4$^+$ Cells. *Virology* **2008**, *381*, 143–154.

46. Garcia, E.; Pion, M.; Pelchen-Matthews, A.; Collinson, L.; Arrighi, J. F.; Blot, G.; Leuba, F.; Escola, J. M.; Demaurex, N.; Marsh, M.; *et al*. HIV-1 Trafficking to the Dendritic Cell-T-Cell Infectious Synapse Uses a Pathway of Tetraspanin Sorting to the Immunological Synapse. *Traffic* **2005**, *6*, 488–501.

47. Mittelbrunn, M.; Yanez-Mo, M.; Sancho, D.; Ursa, A.; Sanchez-Madrid, F. Cutting Edge: Dynamic Redistribution of Tetraspanin CD81 at the Central Zone of the Immune Synapse in Both T Lymphocytes and APC. *J. Immunol.* **2002**, *169*, 6691–6695.

48. Felts, R. L.; Narayan, K.; Estes, J. D.; Shi, D.; Trubey, C. M.; Fu, J.; Hartnell, L. M.; Ruthel, G. T.; Schneider, D. K.; Nagashima, K.; *et al*. 3D Visualization of HIV Transfer at the Virological Synapse between Dendritic Cells and Tcells. *Proc. Natl. Acad. Sci. U.S.A.* **2010**, *107*, 13336–13341.

49. Miller, M. J.; Safrina, O.; Parker, I.; Cahalan, M. D. Imaging the Single Cell Dynamics of CD4+ T Cell Activation by Dendritic Cells in Lymph Nodes. *J. Exp. Med.* **2004**, *200*, 847–856.

50. Mempel, T. R.; Henrickson, S. E.; von Andrian, U. H. T-Cell Priming by Dendritic Cells in Lymph Nodes Occurs in Three Distinct Phases. *Nature* **2004**, *427*, 154–159.

51. Shakhar, G.; Lindquist, R. L.; Skokos, D.; Dudziak, D.; Huang, J. H.; Nussenzweig, M. C.; Dustin, M. L. Stable T Cell-Dendritic Cell Interactions Precede the Development of Both Tolerance and Immunity *in Vivo*. *Nat. Immunol.* **2005**, *6*, 707–714.

52. Yu, H. J.; Reuter, M. A.; McDonald, D. HIV Traffics through a Specialized, Surface-Accessible Intracellular Compartments during Trans-infection of T Cells by Mature Dendritic Cells. *PLoS Pathog.* **2008**, *4*, e1000134.

53. Rong, G.; Wang, H.; Reinhard, B. M. Insights from a Nanoparticle Minuet: Two-Dimensional Membrane Profiling through Silver Plasmon Rulers. *Nano Lett.* **2010**, *10*, 230–238.

54. Wiley, R. D.; Gummuluru, S. Immature Dendritic Cell-Derived Exosomes Can Mediate HIV-1 Trans-infection. *Proc. Natl. Acad. Sci. U.S.A.* **2006**, *103*, 738–743.